PHOTONICS Research

Transport of a topologically protected photonic waveguide on-chip

Sai Yan,[1,2] Jingnan Yang,[3] Shushu Shi,[1,2] Zhanchun Zuo,[1] Can Wang,[1,4,5] and Xiulai Xu[3,*]

[1]Beijing National Laboratory for Condensed Matter Physics, Institute of Physics, Chinese Academy of Sciences, Beijing 100190, China
[2]CAS Center for Excellence in Topological Quantum Computation and School of Physical Sciences, University of Chinese Academy of Sciences, Beijing 100049, China
[3]State Key Laboratory for Mesoscopic Physics and Frontiers Science Center for Nano-optoelectronics, School of Physics, Peking University, Beijing 100871, China
[4]Songshan Lake Materials Laboratory, Dongguan 523808, China
[5]e-mail: canwang@iphy.ac.cn
*Corresponding author: xlxu@pku.edu.cn

Received 16 January 2023; revised 7 April 2023; accepted 9 April 2023; posted 11 April 2023 (Doc. ID 485676); published 26 May 2023

We propose a design on integrated optical devices on-chip with an extra width degree of freedom by using a photonic crystal waveguide with Dirac points between two photonic crystals with opposite valley Chern numbers. With such an extra waveguide, we demonstrate numerically that the topologically protected photonic waveguide retains properties of valley-locking and immunity to defects. Due to the design flexibility of the width-tunable topologically protected photonic waveguide, many unique on-chip integrated devices have been proposed, such as energy concentrators with a concentration efficiency improvement of more than one order of magnitude, and a topological photonic power splitter with an arbitrary power splitting ratio. The topologically protected photonic waveguide with the width degree of freedom could be beneficial for scaling up photonic devices, and provides a flexible platform to implement integrated photonic networks on-chip.

https://doi.org/10.1364/PRJ.485676

1. INTRODUCTION

Due to the advantages of low energy cost and broad bandwidth in processing information, on-chip nanophotonic devices have been widely studied in recent years [1–4], becoming an important platform for constructing all-optical connectivity, all-optical computing, and all-optical networks [1,2,5–7]. However, imperfect fabrication of nanophotonic devices is often unavoidable, which lowers the performance of the devices [8]. The emergence of topological photonics has provided a way to solve the functional influences of fabrication errors of nanophotonic devices [8–11], and shows great potential to control the propagation of light.

In particular, the topological edge states that exist at the interface between two valley photonic crystals (PhCs) with opposite valley Chern numbers or band inversion exhibit novel properties, such as robustness against defects and unidirectional transmission [9–21]. So far, a large number of on-chip topological photonic devices exhibiting robustness have been demonstrated, such as topological lasers [22–25], topological optical switches [26–28], topologically protected photonic waveguides (TPPWs) [15,29–34], topological filters [35–38], and topological sensors [39]. Most of these topological nanophotonic devices show better performance. For example, TPPWs can have larger operating bandwidths, lower propagation losses, smaller footprints, and higher operation efficiency at telecommunication wavelengths [10,12,15,16,18,40,41]. However, since topological edge states are usually localized at the interface between valley PhCs [9–19,40], the width of the TPPW is not tunable. A tunable width of waveguides provides not only a degree of freedom (DOF) in designing photonic devices [3,7,42,43], but also an opportunity to interface with other photonic devices with high flexibility. Therefore, it is highly desired to introduce the width DOF in TPPWs. The introduction of width DOF has been proposed and experimentally demonstrated for devices working in the microwave regime [42,43]. To implement on-chip integrated optical networks [44–47], here we expand it to the near infrared optical wavelength range.

In this paper, we propose to introduce width DOF into a TPPW to more flexibly manipulate light transport. PhCs with Dirac points are sandwiched by two PhCs with opposite valley Chern numbers, which constitute a TPPW with high flexibility. The TPPW with the introduction of width DOF retains the characteristics of gapless dispersion, valley-momentum locking and robustness to defects. Taking advantage of these properties, we design a multi-level energy concentrator by abruptly reducing the waveguide width. Energy intensity is enhanced by 2.48 to 23.38 times by putting a photonic structure with a bandgap as a mirror at the end of the waveguide. The photonic energy

concentrator could be used for applications in energy convergences [48] and nonlinear optics [49,50]. In addition, a topological photonic power splitter with arbitrary coupling ratios is also proposed by introducing width DOF, which could be useful for scaling up photonic devices on-chip with low losses.

2. STRUCTURE DESIGN

The topological valley PhC here contains three domains, A, B, and C [Fig. 1(a)], which are composed of a honeycomb lattice with two different sizes of triangular airholes, as shown in the insets of Fig. 1(a). The side lengths of the triangular airholes are described by L_1 and L_2. Dirac degeneracy exists in K valley of the PhCs in the B domain when the two triangular airholes are the same size ($L_1 = L_2 = 82$ nm). When $L_1 \neq L_2$, the spatial inversion of PhCs in the A and C domains is broken with the formation of a bandgap [as shown in Fig. 1(b)]. PhCs in the A or C domain show nonzero Berry curvatures, with opposite signs at K and K' valleys. Due to the time-reversal symmetry, the Berry curvature is equal to zero by integrating over the entire Brillouin zone (BZ). It is worth noting that the valley Chern number is nonzero since we need only to integrate the Berry curvature over half of the BZ around the K/K' valley [15,16]. The inset of Fig. 1(a) shows the rhomboid units of three topologically distinct PhCs. The larger triangular airholes in the PhC of the A domain (blue) and C domain (red) are oppositely orientated. The sign of the Berry curvature at each valley will be reversed by swapping the sizes of the two triangular airholes. Therefore, PhCs in the A and C domains appear with opposite valley Chern numbers and different valley phases. To illustrate the phase transition visually, we simulated the z component of the magnetic field (H_z) phase profiles of the PhCs in the A and C domains at K point. Figures 1(c) and 1(f) show valley phase locking with a clockwise vortex at K point in the upper band (321.11 THz) of PhCs in the A domain and the lower band (293.14 THz) of PhCs in the C domain, respectively. Figures 1(d) and 1(e) show another valley phase locking with an anticlockwise vortex at K point in the lower band of PhCs in the A domain and the upper band of PhCs in the C domain, respectively. The red and blue arrows point to the phase profile increasing by 2π phase either anticlockwise or clockwise around the center of the unit cell. Due to the time-reversal symmetry, the counterparts have opposite vertices at K' point. The topological edge states exist in the interface between two topologically distinct PhCs with opposite optical vortices [9–19,40]. By introducing a PhC in the B domain into the interface, the topological edge states still exist.

Figure 2(a) depicts the projected band structure of the TPPW with the number of layers $x = 5$ of B domain (A|B_5|C). The red line inside the bandgap shows a gapless band. With a pair of opposite group velocities connected to K and K', the gapless band has the same valley-locking property as the edge state in the A|C domain interface. This state is referred to as the topological valley-locked waveguide state (TVWS). In addition, there are higher-order non-topological waveguide states (NTWSs) with gapped dispersion, represented by the symbols 0^+th, 0^-th, 1^+st, and 1^-st [as shown in Fig. 2(a)]. It is worth noting that different from TVWSs, NTWSs are gapped and lack the valley-locking property. The gap between the 0^+th band and the 0^-th band is called the topological frequency window [light gray area in Fig. 2(a)], where only the TVWS exists. From Fig. 2(b), we can see that the width of the topological frequency window varies with the number of layers x in B domain. As the number of layers x in B domain increases, the width of the topological frequency window narrows with higher-order NTWSs such as 1^+st, 1^-st, 2^+nd, and 2^-nd. In the extreme case when layer x in the B domain is large enough, the topological frequency window eventually closes and the bulk-edge correspondence between A and C domains gradually weakens. As a result, the waveguide band structure becomes the bulk band structure of the B domain.

To explain the origin of the topological guided mode in TVWSs, we turn our attention to the $k \cdot p$ perturbation method [11,51,52]. The effective Hamiltonian around the K valley, which represents PhCs in the A, B, and C domains, can be written as

$$\delta H_K(\delta k) = c_D \delta k_x \sigma_x + c_D \delta k_y \sigma_y + m c_D^2 \sigma_z, \quad (1)$$

where m is the effective mass with $m < 0$ for A crystal, $m = 0$ for B crystal, and $m > 0$ for C crystal; c_D is the group velocity or the slope of the linear Dirac cone in B crystal, $\delta k = k - k_K$ is the displacement of wave vector k to the K valley, and σ_i ($i = x, y, z$) are Pauli matrices. It is obvious that the effective Hamiltonian around the K' valley can be obtained by applying

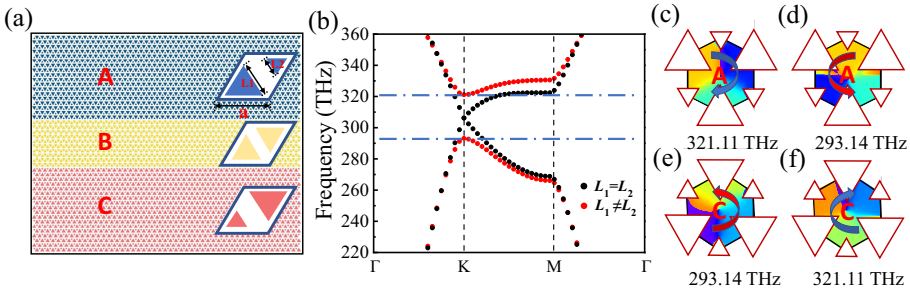

Fig. 1. (a) Schematic diagram of the topologically protected photonic waveguide (TPPW). The TPPW consists of three domains, A|B_x|C, where the unit cells of PhCs in A and C domains have broken-inversion symmetry and that in B domain has inversion symmetry. The structure parameters are $L_1 = 196$ nm and $L_2 = 84$ nm for A domain ($L_1 = L_2 = 151.2$ nm for B domain, $L_1 = 84$ nm and $L_2 = 196$ nm for C domain), lattice constant $a = 280$ nm, and thickness of the structure $d = 150$ nm. (b) Band diagrams of PhC in B domain ($L_1 = L_2$) with Dirac points, and band diagrams of PhC in A or C domain ($L_1 \neq L_2$) with a bandgap. (c)–(f) H_z phase profiles of PhC in A domain and PhC in C domain at K point in the upper (321.11 THz) and lower (293.14 THz) bands.

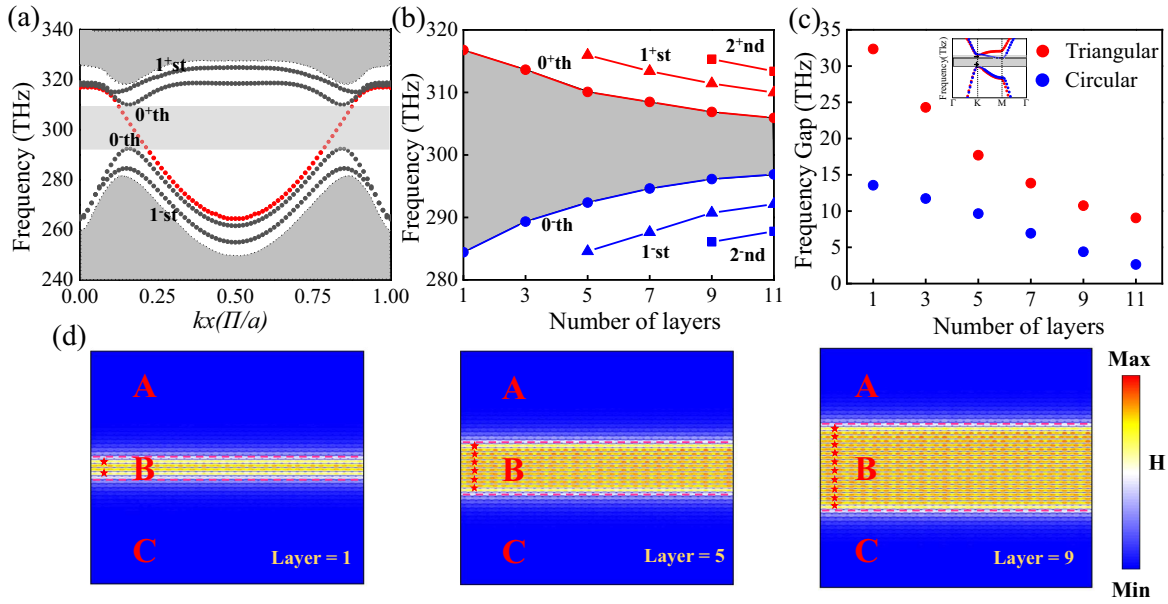

Fig. 2. (a) Band diagram of A|B_5|C waveguide. The red dotted lines show the topological edge state. The zeroth and first bands, marked with black lines, are other gapped waveguide states. The light gray area in the bulk gap of A or C domain is referred to as the topological frequency window. (b) Width of the topological frequency window as a function of the number of layers x in B domain. (c) Frequency gap of the topological frequency window of valley-locked waveguide consisting of honeycomb lattices with two sizes of triangular and circular airholes as a function of the number of layers x in B domain. Inset: band diagrams with different shapes. (d) H_z field distributions of three straight TPPWs with $x = 1$, 5, and 9.

a time reversal operation on the Hamiltonian at K valley. From the eigenvalue equation $\delta H_K \phi = \delta\omega\phi$, we can obtain the dispersion relation

$$\delta^2\omega = c_D^2(\delta^2 k_x + \delta^2 k_y) + m^2 c_D^4, \tag{2}$$

which describes the dispersion relation of A, B, and C crystals. Additionally, the topological guided mode ϕ_{ABC} in the TPPW exponentially attenuates along the $+Y$ direction in A domain and along the $-Y$ in C domain [43,53]. A specific solution with $\delta\omega = c_D\delta k_x$ can be obtained, where the slope c_D is identical to the bulk states in B domain ($\delta\omega = \pm c_D\delta k$). Therefore, we can conclude that the topological guided mode is a combination of the valley edge state at the A|C domain interface and the bulk states in B domain [42,43,53–55].

The frequency window of the PhC waveguide directly affects the performance of the photonic device, where a wider frequency window will improve the operating bandwidth of the photonic devices. We compare the width of the topological frequency window of a valley-locked waveguide consisting of honeycomb lattices with two triangular and two circular airholes [as shown in Fig. 2(c)]. In the topological valley PhC with circular airholes, the radii of the circular airholes in A/C domains are 66.7 and 42 nm, respectively. The radius of the circular airhole in B domain is 54 nm. The lattice constant is 280 nm. We can see that a valley-locked waveguide with a honeycomb lattice with two triangular airholes has a much larger topological frequency window than one with a honeycomb lattice with two circular airholes, regardless of the number of layers in B domain. This is due to the difference in the band structures of PhCs consisting of a honeycomb lattice with two triangular airholes and PhCs consisting of a honeycomb lattice with two circular airholes. The former is a direct bandgap, while the latter is an indirect bandgap, as shown in the inset in Fig. 2(c). The indirect bandgap of a honeycomb lattice with two circular airholes might be due to the smaller effective refraction index than that with two triangular airholes, which also modifies the dispersion in the gap. From a practical point of view, a TPPW consisting of PhCs with a direct bandgap has a larger topological frequency window than one with an indirect bandgap, which is important, particularly for devices with self-assembled quantum dots with a large size distribution [40]. Therefore, we choose PhCs consisting of a honeycomb lattice with two different sizes of triangular airholes to construct TPPWs in this work. In addition, the bandwidth of the devices is also related to the size of bandgap of the PhCs that make up the device and the waveguide interfaces that constitute the device [56]. As the size of the bandgap of the PhC increases, i.e., L_1/L_2, the bandwidth of the corresponding topologically protected waveguide becomes larger. The maximum achievable bandwidth of the topologically protected waveguide is approximately 45 THz when experimental fabrication is considered. With all the above reasons considered, we choose large triangle and small triangle side lengths of 196 and 84 nm, respectively, and zigzag interfaces.

How the topological guide modes transport in the TPPW with width DOF is very important for subsequent device designs. In the simplest cases, we put red-marked point sources inside three waveguides with $x = 1$, 5, 9, to excite the TVWSs. Figure 2(d) shows the H_z field map of three TVWSs with $x = 1$, 5, 9 at 302.08 THz. From the three simulated H_z field maps, we can get energy confined to B domain to propagate between A and C domains regardless of the number of layers in B domain, which makes it possible to control the TVWS transport by varying the TPPW width.

3. PROPERTIES OF TVWSs

To demonstrate the robustness against defects of TVWSs, we introduce four distinct defects into B domain of the waveguides. The four structural defects are bulging, indentation, bending, and disorder. Figures 3(a)–3(d) display the simulated field distributions for the four waveguides with four types of structural defects at a frequency of 302.08 THz. We put the point source into input port 1 to excite TVWSs and a monitor into the terminal of output port 4 to receive the signal. TVWSs can transport forward while passing defects due to the protection of topology. We compare the energy intensity of the waveguide without any defects with the transmission fields measured at the positions labeled by blue dots at the exits of the four waveguides in Figs. 3(a)–3(d). As shown in Fig. 3(e), regardless of the existence of defects, TVWS propagation within the topological frequency window (shaded region) stays highly consistent with that of the topological frequency window without the defect. On the contrary, outside the shaded area, the simulated field intensity can become largely different due to the existence of other high-order edge states. The phase of TVWSs transmitted in the waveguide without defects is shown in Fig. 3(f), while the phase of TVWSs propagating in the waveguide shown in Fig. 3(a) after passing through the defects is shown in Fig. 3(g). We can see that the phases of two TVWSs are highly consistent. Figures 3(b)–3(d) are also consistent with the two phase diagrams above, which implies that the propagation of TVWSs is immune to different defects [54].

To show the existence of the valley-locking effect, a valley-locked topological channel intersection is simulated based on TVWSs. The device's configuration, as illustrated in Figs. 4(a) and 4(b), consists of five domains separated by the red dotted line, with the number of layers $x = 5$ in B domain. We set ports 1–4 at the terminals of B domain, placing point sources at port 1 as input ports to excite TVWSs, while ports 2–4 are considered as output ports to receive signals. The field distributions are at 302.08 THz as shown in Figs. 4(a) and 4(b). Since TVWSs propagate in A|B_x|C and C|B_x|A waveguides instead of A|B_x|A and C|B_x|C waveguides [53], TVWSs transmitted to output ports 2 and 3 are suppressed, and TVWSs locked to the *K*-valley propagate only along channel toward port 4, as in the case of Fig. 4(a). In contrast, TVWSs locked to the *K*-valley propagate along the channel toward ports 2 and 3 but not port 4 because TVWSs from the A|B_x|C and C|B_x|A waveguides are locked to the opposite valley, as shown in Fig. 4(b). To explain the splitting effect of TVWSs more intuitively, we put the monitors on the light blue dashed lines as shown in Figs. 4(a) and 4(b) at ports 2, 3, and 4 to obtain the transmission spectra. Figure 4(c) shows that TVWSs mostly propagate along the channel toward port 4 in the topological frequency window with a transmittance of 98%. Figure 4(d) shows that TVWSs barely propagate along the channel toward port 4 in the topological frequency window. It is worth noting that the transmittances of TVWSs through ports 2 and 3 are not the same due to the different types of waveguide interfaces. These simulation results indicate that TVWSs locked into different valleys propagate only in the corresponding channels with the extra width DOF.

4. APPLICATIONS OF TVWSs

To realize an on-chip optical integration network with a small footprint and high degree of integration, the high-efficiency energy output of an on-chip optical integration network is one of the remaining challenges. With the robustness and valley-locking properties of TVWSs discussed above, we design an energy concentrator for energy harvesting. Figure 5(a) shows the schematic diagram of the topological concentrator. The first half of the topological concentrator consists of a waveguide with a sharp decrease in the number of layers in B domain from 9 to 0.5. The sharp turns in the system are fixed at 60° or 120°. We place point sources marked as red stars to excite

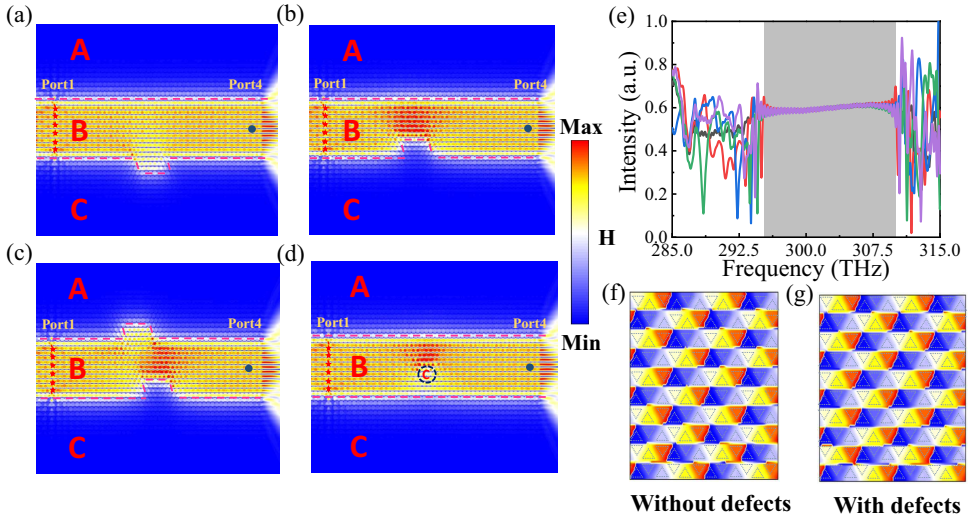

Fig. 3. (a)–(d) Simulated photonic H_z field distributions at 302.08 THz in waveguides with four different defects: bulging, indentation, bending, and disorder. (e) Field intensities measured at the points represented by blue dots near the exits of the four waveguides with defects in (a)–(d). The black line is the field intensity of a waveguide without defects. The great consistency of field intensities in the topological frequency windows indicates the immunity of TVWSs to defects. H_z phase diagrams of TVWSs after transmission (f) without and (g) with defects.

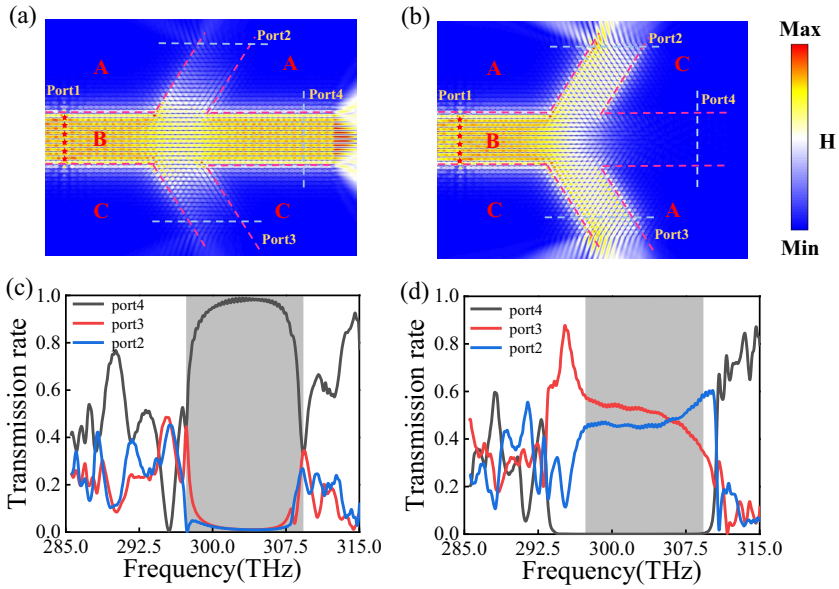

Fig. 4. (a), (b) Simulated photonic H_z field distributions under the excitation of point sources at the input port 1 for two different configurations at 302.08 THz. Three ports labeled 2, 3, and 4 are located in B domain. (c), (d) Transmittance of TVWSs through port 2, port 3, and port 4 for (a) and (b), respectively.

TVWSs. When TVWSs enter the narrow part of B domain, backscattering hardly occurs due to the valley-locking property [43,53]. The energy converges to the narrow part of B domain, called first-order convergence. The waveguide with $x = 0.5$ in B domain is terminated by a mirror made up of a PhC, which constitutes the latter half of the topological concentrator. The PhC structure as a mirror in Fig. 5(a) is composed of a periodic array of a square lattice with a square airhole. The length of the square airhole is 204.8 nm, lattice constant is 320 nm, and thickness of the structure is 150 nm. The bandgap of the mirror ranges from 283.6 to 323.9 THz, while the bandwidth of the device in Fig. 5(a) ranges from 296.129 to 306.881 THz. Therefore, when TVWSs within the bandwidth propagate along the topologically protected waveguide to the end, TVWSs cannot propagate inside mirrors. When TVWSs transport to the terminal of the waveguide, the energy is further gathered due to the existence of the mirror and the near-conservation of the valley [9,12,57]. As shown in Fig. 5(b), a large amount of energy is concentrated in a very small cavity, called second-order convergence. To quantitatively assess the ability of energy convergence, the intensity profiles are shown by simulations in Fig. 5(c) along the black, red, and blue dotted lines in Fig. 5(a). It can be seen that from the inset of Fig. 5(c) the energy intensity along the red line is 2.48 times higher than the energy intensity along the black line. It is worth noting that the energy intensity along the blue line is 23.38 times higher than that along the black line, as shown in Fig. 5(c). The energy concentrator without backscattering could be used in the integrated photonic circuit. The energy concentrator is essentially a cavity with a very small mode volume, as shown in Fig. 5(b), which could be used for studying cavity quantum electrodynamics and low threshold lasers [24,40,50,58,59].

Figure 5(d) shows a topological photonic power splitter. By introducing B domain into the A|C boundary, it provides a new DOF for the power splitter. We design a relatively simple topological photonic power splitter to illustrate how the new DOF comes into play. As shown in Fig. 5(d), the structural design of the power splitter is like that in Fig. 4(b), and the difference is that the output ports are on the right side of the structure. To unify the variables, the number of layers in the B domain of the output port is designed to be one. We place red-marked point sources in Fig. 5(d) to excite TVWSs, which propagate to the output port along the top and bottom waveguides. The number of layers in the B domain of the top waveguide is equal to 1 ($x_1 = 1$), and the number of layers in the bottom waveguide is equal to 2 ($x_2 = 2$). While maintaining the position of the bottom waveguide, we can obtain more splitting ratios by moving the position of the upper waveguide [60]. It should be noted that simply changing the relative positions of the upper and bottom waveguides does not result in more splitting ratios. Instead, by simultaneously adjusting the new adjustment DOF, which includes the layer numbers of the upper and bottom waveguides and their relative positions, we can obtain the topological photonic power splitter with an arbitrary power splitting ratio. Figure 5(e) shows the field distribution for the difference between the relative positions of the top and bottom waveguides equal to $4a$ (a is the lattice constant). The field intensity at port 1 is higher than that at port 2. As shown in Fig. 5(f), the power splitting ratio of the device shows different power splitting cases as the top waveguide position shifts. We define the shift distance as zero for the case in Fig. 5(d). As the top waveguide is moved along the port 1 direction with lattice constant a as the moving unit, the power splitting ratio of the device shows a nearly linear variation. As the number of layers of the bottom waveguide increases, the top waveguide moving range increases, and finer power splitting ratios can be obtained. Based on the results, the topological photonic power splitter with arbitrary power splitting ratios requires only a simple

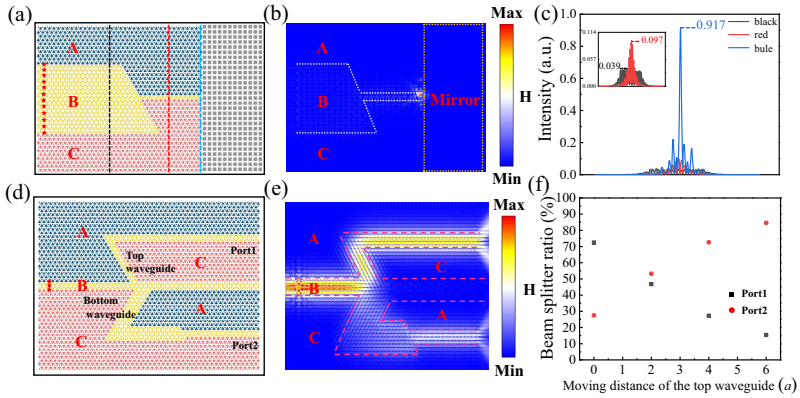

Fig. 5. (a) Schematic of a topological concentrator. The width of B domain abruptly changes from 9 to 0.5 layers in the middle of the device. The waveguide with $x = 0.5$ in the B domain is terminated by a mirror made up of a photonic crystal structure. Red stars: point sources. (b) Simulated H field distributions in the topological concentrator at 302.08 THz. (c) Simulated intensity profiles along black, red, and blue dashed lines in (a). (d) Schematic of a topological photonic power splitter. The width of B domain of the top waveguide is one and that of bottom waveguide is two. Red stars: point sources. (e) Simulated H field distributions in the topological photonic power splitter at 302.08 THz. (f) The power splitting ratio of the device varies with the top waveguide shift in units of the lattice constant a.

adjustment of the number of layers of the top and bottom waveguides and their relative positions, which is important for integrated photonic devices on-chip.

Design parameters of all the devices mentioned above are experimentally feasible. In our work, the crystal constant in our design is 280 nm, the side lengths of the triangular airholes are 196, 151.2, and 84 nm, and the thickness is 150 nm, which corresponds to a center operating frequency of 300 THz for valley-locked waveguides. The devices with a thickness of 150 nm do not need a deep etching process, without the aspect ratio fabrication challenge compared to the devices for developing 6G technologies [28,34,39,56]. PhC waveguide structures with very similar design parameters have been fabricated and demonstrated in various applications, such as GaAs valley PhC waveguides with light-emitting InAs quantum dots [61], protecting transport at telecommunication wavelengths [15], and broadband Purcell enhancement [40]. Therefore, the device design with topologically protected waveguides is feasible and can be experimentally implemented.

5. CONCLUSION

In summary, we proposed a design on integrated optical devices by using topological valley-locked waveguides with the introduction of width DOF to manipulate the transport of light. First we demonstrated that TVWSs possess gapless dispersions, momentum-valley locking, and robustness. Then valley-locked energy concentrators and energy power splitters with arbitrary power splitting ratios were designed on-chip with higher flexibility by introducing width DOF, which provides opportunities for designing various kinds of devices for different functions. Comparing with previous topological waveguides, TPPWs with the width DOF enable flexible design of on-chip integrated devices. More importantly, it can be flexibly interfaced with existing photonic devices, which promotes the development of on-chip integrated optical networks.

Funding. National Key Research and Development Program of China (2021YFA1400700); National Natural Science Foundation of China (62025507, 11934019, 92250301, 11721404, 62175254, 12174437, 12204020); Chinese Academy of Sciences (XDB28000000); China Postdoctoral Science Foundation (2022M710234).

Disclosures. The authors declare no conflicts of interest.

Data Availability. Data underlying the results presented in this paper are not publicly available at this time but may be obtained from the authors upon reasonable request.

REFERENCES

1. C. Sun, M. T. Wade, Y. Lee, J. S. Orcutt, L. Alloatti, M. S. Georgas, A. S. Waterman, J. M. Shainline, R. R. Avizienis, S. Lin, B. R. Moss, R. Kumar, F. Pavanello, A. H. Atabaki, H. M. Cook, A. J. Ou, J. C. Leu, Y.-H. Chen, K. Asanović, R. J. Ram, M. A. Popović, and V. M. Stojanović, "Single-chip microprocessor that communicates directly using light," Nature **528**, 534–538 (2015).
2. P. Kok, W. J. Munro, K. Nemoto, T. C. Ralph, J. P. Dowling, and G. J. Milburn, "Linear optical quantum computing with photonic qubits," Rev. Mod. Phys. **79**, 135–174 (2007).
3. S. Xiao, S. Wu, X. Xie, J. Yang, W. Wei, S. Shi, F. Song, S. Sun, J. Dang, L. Yang, Y. Wang, Z. Zuo, T. Wang, J. Zhang, and X. Xu, "Position-dependent chiral coupling between single quantum dots and cross waveguides," Appl. Phys. Lett. **118**, 091106 (2021).
4. S. Shi, S. Xiao, and X. Xu, "Chiral optical transport of quantum dots with different diamagnetic behaviors in a waveguide," Acta Phys. Sin. **71**, 067801 (2022).
5. Y. Ji, J. Zhang, Y. Zhao, X. Yu, J. Zhang, and X. Chen, "Prospects and research issues in multi-dimensional all optical networks," Sci. China Inf. Sci. **59**, 101301 (2016).
6. H. J. Caulfield and S. Dolev, "Why future supercomputing requires optics," Nat. Photonics **4**, 261–263 (2010).
7. S. Xiao, S. Wu, X. Xie, J. Yang, W. Wei, S. Shi, F. Song, J. Dang, S. Sun, L. Yang, Y. Wang, S. Yan, Z. Zuo, T. Wang, J. Zhang, K. Jin, and X. Xu, "Chiral photonic circuits for deterministic spin transfer," Laser Photon. Rev. **15**, 2100009 (2021).
8. X. Xie, J. Dang, S. Yan, W. Zhang, H. Hao, S. Xiao, S. Shi, Z. Zuo, H. Ni, Z. Niu, X. Zhang, C. Wang, and X. Xu, "Optimization and

robustness of the topological corner state in second-order topological photonic crystals," Opt. Express **29**, 30735–30750 (2021).
9. T. Ma and G. Shvets, "All-Si valley-Hall photonic topological insulator," New J. Phys. **18**, 025012 (2016).
10. Z. Gao, Z. Yang, F. Gao, H. Xue, Y. Yang, J. Dong, and B. Zhang, "Valley surface-wave photonic crystal and its bulk/edge transport," Phys. Rev. B **96**, 201402 (2017).
11. X. Wu, Y. Meng, J. Tian, Y. Huang, H. Xiang, D. Han, and W. Wen, "Direct observation of valley-polarized topological edge states in designer surface plasmon crystals," Nat. Commun. **8**, 1304 (2017).
12. F. Gao, H. Xue, Z. Yang, K. Lai, Y. Yu, X. Lin, Y. Chong, G. Shvets, and B. Zhang, "Topologically protected refraction of robust kink states in valley photonic crystals," Nat. Phys. **14**, 140–144 (2018).
13. J. Noh, S. Huang, K. P. Chen, and M. C. Rechtsman, "Observation of photonic topological valley Hall edge states," Phys. Rev. Lett. **120**, 063902 (2018).
14. X. Chen, W. Deng, J. Lu, and J. Dong, "Valley-controlled propagation of pseudospin states in bulk metacrystal waveguides," Phys. Rev. B **97**, 184201 (2018).
15. M. I. Shalaev, W. Walasik, A. Tsukernik, Y. Xu, and N. M. Litchinitser, "Robust topologically protected transport in photonic crystals at telecommunication wavelengths," Nat. Nanotechnol. **14**, 31–34 (2019).
16. X. He, E. Liang, J. Yuan, H. Qiu, X. Chen, F. Zhao, and J. Dong, "A silicon-on-insulator slab for topological valley transport," Nat. Commun. **10**, 872 (2019).
17. Q. Chen, L. Zhang, M. He, Z. Wang, X. Lin, F. Gao, Y. Yang, B. Zhang, and H. Chen, "Valley-Hall photonic topological insulators with dual-band kink states," Adv. Opt. Mater. **7**, 1900036 (2019).
18. L. Zhang, Y. Yang, M. He, H.-X. Wang, Z. Yang, E. Li, F. Gao, B. Zhang, R. Singh, J.-H. Jiang, and H. Chen, "Valley kink states and topological channel intersections in substrate-integrated photonic circuitry," Laser Photon. Rev. **13**, 1900159 (2019).
19. Y. Yang, Y. Yamagami, X. Yu, P. Pitchappa, J. Webber, B. Zhang, M. Fujita, T. Nagatsuma, and R. Singh, "Terahertz topological photonics for on-chip communication," Nat. Photonics **14**, 446–451 (2020).
20. A. Kumar, M. Gupta, P. Pitchappa, N. Wang, M. Fujita, and R. Singh, "Terahertz topological photonic integrated circuits for 6G and beyond: a perspective," J. Appl. Phys. **132**, 140901 (2022).
21. A. Kumar, M. Gupta, and R. Singh, "Topological integrated circuits for 5G and 6G," Nat. Electron. **5**, 261–262 (2022).
22. Y. Gong, S. Wong, A. J. Bennett, D. L. Huffaker, and S. S. Oh, "Topological insulator laser using valley-Hall photonic crystals," ACS Photon. **7**, 2089–2097 (2020).
23. X. Liu, L. Zhao, D. Zhang, and S. Gao, "Topological cavity laser with valley edge states," Opt. Express **30**, 4965–4977 (2022).
24. W. Zhang, X. Xie, H. Hao, J. Dang, S. Xiao, S. Shi, H. Ni, Z. Niu, C. Wang, K. Jin, X. Zhang, and X. Xu, "Low-threshold topological nanolasers based on the second-order corner state," Light Sci. Appl. **9**, 109 (2020).
25. H. Zhong, Y. Li, D. Song, Y. V. Kartashov, Y. Zhang, Y. Zhang, and Z. Chen, "Topological valley Hall edge state lasing," Laser Photon. Rev. **14**, 2000001 (2020).
26. N. A. Riza and S. Yuan, "Reconfigurable wavelength add-drop filtering based on a Banyan network topology and ferroelectric liquid crystal fiber-optic switches," J. Lightwave Technol. **17**, 1575–1584 (1999).
27. H. Qi, X. Wang, X. Hu, Z. Du, J. Yang, Z. Yu, S. Ding, S. Chu, and Q. Gong, "All-optical switch based on novel physics effects," J. Appl. Phys. **129**, 210906 (2021).
28. A. Kumar, M. Gupta, P. Pitchappa, T. C. Tan, U. Chattopadhyay, G. Ducournau, N. Wang, Y. Chong, and R. Singh, "Active ultrahigh-Q (0.2×10^6) THz topological cavities on a chip," Adv. Mater. **34**, 2202370 (2022).
29. M. J. Mehrabad, A. P. Foster, R. Dost, E. Clarke, P. K. Patil, A. M. Fox, M. S. Skolnick, and L. R. Wilson, "Chiral topological photonics with an embedded quantum emitter," Optica **7**, 1690–1696 (2020).
30. F. Haldane and S. Raghu, "Possible realization of directional optical waveguides in photonic crystals with broken time-reversal symmetry," Phys. Rev. Lett. **100**, 013904 (2008).
31. Z. Wang, Y. Chong, J. D. Joannopoulos, and M. Soljačić, "Observation of unidirectional backscattering-immune topological electromagnetic states," Nature **461**, 772–775 (2009).
32. K. Fang, Z. Yu, and S. Fan, "Realizing effective magnetic field for photons by controlling the phase of dynamic modulation," Nat. Photonics **6**, 782–787 (2012).
33. X. Xi, K. Ye, and R. Wu, "Topological photonic crystal of large valley Chern numbers," Photon. Res. **8**, B1–B7 (2020).
34. A. Kumar, M. Gupta, P. Pitchappa, N. Wang, P. Szriftgiser, G. Ducournau, and R. Singh, "Phototunable chip-scale topological photonics: 160 Gbps waveguide and demultiplexer for THz 6G communication," Nat. Commun. **13**, 5404 (2022).
35. L. Gu, Q. Yuan, Q. Zhao, Y. Ji, Z. Liu, L. Fang, X. Gan, and J. Zhao, "A topological photonic ring-resonator for on-chip channel filters," J. Lightwave Technol. **39**, 5069–5073 (2021).
36. X. Chen, W. Deng, F. Shi, F. Zhao, M. Chen, and J. Dong, "Direct observation of corner states in second-order topological photonic crystal slabs," Phys. Rev. Lett. **122**, 233902 (2019).
37. X.-L. Lü and H. Xie, "Spin filters and switchers in topological-insulator junctions," Phys. Rev. Appl. **12**, 064040 (2019).
38. J. Yang, X. Lü, C. Zhang, and H. Xie, "Topological spin–valley filtering effects based on hybrid silicene-like nanoribbons," New J. Phys. **22**, 053034 (2020).
39. A. Kumar, M. Gupta, P. Pitchappa, Y. J. Tan, N. Wang, and R. Singh, "Topological sensor on a silicon chip," Appl. Phys. Lett. **121**, 011101 (2022).
40. X. Xie, S. Yan, J. Dang, J. Yang, S. Xiao, Y. Wang, S. Shi, L. Yang, D. Dai, Y. Yuan, N. Luo, T. Cui, G. Chi, Z. Zuo, B.-B. Li, C. Wang, and X. Xu, "Topological cavity based on slow-light topological edge mode for broadband Purcell enhancement," Phys. Rev. Appl. **16**, 014036 (2021).
41. X. Liu, J. Huang, H. Chen, Z. Qian, J. Ma, X. Sun, S. Fan, and Y. Sun, "Terahertz topological photonic waveguide switch for on-chip communication," Photon. Res. **10**, 1090–1096 (2022).
42. M. Wang, R. Zhang, L. Zhang, D. Wang, Q. Guo, Z. Zhang, and C. T. Chan, "Topological one-way large-area waveguide states in magnetic photonic crystals," Phys. Rev. Lett. **126**, 067401 (2021).
43. Q. Chen, L. Zhang, F. Chen, Q. Yan, R. Xi, H. Chen, and Y. Yang, "Photonic topological valley-locked waveguides," ACS Photon. **8**, 1400–1406 (2021).
44. R. Nagarajan, C. H. Joyner, R. P. Schneider, J. S. Bostak, T. Butrie, A. G. Dentai, V. G. Dominic, P. W. Evans, M. Kato, M. Kauffman, D. J. H. Lambert, S. K. Mathis, A. Mathur, R. H. Miles, M. L. Mitchell, M. J. Missey, S. Murthy, A. C. Nilsson, F. H. Peters, S. C. Pennypacker, J. L. Pleumeekers, R. A. Salvatore, R. K. Schlenker, R. B. Taylor, H.-S. Tsai, M. F. Van Leeuwen, J. Webjorn, M. Ziari, D. Perkins, J. Singh, S. G. Grubb, M. S. Reffle, D. G. Mehuys, F. A. Kish, and D. F. Welch, "Large-scale photonic integrated circuits," IEEE J. Sel. Top. Quantum Electron. **11**, 50–65 (2005).
45. T. L. Koch and U. Koren, "Semiconductor photonic integrated circuits," IEEE J. Quantum Electron. **27**, 641–653 (1991).
46. G. Son, S. Han, J. Park, K. Kwon, and K. Yu, "High-efficiency broadband light coupling between optical fibers and photonic integrated circuits," Nanophotonics **7**, 1845–1864 (2018).
47. T. Komljenovic, M. Davenport, J. Hulme, A. Y. Liu, C. T. Santis, A. Spott, S. Srinivasan, E. J. Stanton, C. Zhang, and J. E. Bowers, "Heterogeneous silicon photonic integrated circuits," J. Lightwave Technol. **34**, 20–35 (2016).
48. R. Piao and D. Zhang, "Ultra-broadband perfect absorber based on nanoarray of titanium nitride truncated pyramids for solar energy harvesting," Physica E **134**, 114829 (2021).
49. Z. Lan, J. W. You, and N. C. Panoiu, "Nonlinear one-way edge-mode interactions for frequency mixing in topological photonic crystals," Phys. Rev. B **101**, 155422 (2020).
50. X. Xie, W. Zhang, X. He, S. Wu, J. Dang, K. Peng, F. Song, L. Yang, H. Ni, Z. Niu, C. Wang, K. Jin, X. Zhang, and X. Xu, "Cavity quantum electrodynamics with second-order topological corner state," Laser Photon. Rev. **14**, 1900425 (2020).
51. Á. Notomi, "Theory of light propagation in strongly modulated photonic crystals: refractionlike behavior in the vicinity of the photonic band gap," Phys. Rev. B **62**, 10696 (2000).
52. J. Mei, Y. Wu, C. T. Chan, and Z.-Q. Zhang, "First-principles study of Dirac and Dirac-like cones in phononic and photonic crystals," Phys. Rev. B **86**, 035141 (2012).

53. M. Wang, W. Zhou, L. Bi, C. Qiu, M. Ke, and Z. Liu, "Valley-locked waveguide transport in acoustic heterostructures," Nat. Commun. **11**, 3000 (2020).
54. J. Wang, Z. Zhang, S. Yu, H. Ge, K. Liu, T. Wu, X. Sun, L. Liu, H. Chen, C. He, M. Lu, and Y. Chen, "Extended topological valley-locked surface acoustic waves," Nat. Commun. **13**, 1324 (2022).
55. Z. Chen, X. Wang, C. Lim, and F. Shi, "Robust large-area elastic transverse wave transport in active acoustic metamaterials," J. Appl. Phys. **131**, 185112 (2022).
56. Y. J. Tan, W. Wang, A. Kumar, and R. Singh, "Interfacial topological photonics: broadband silicon waveguides for THz 6G communication and beyond," Opt. Express **30**, 33035–33047 (2022).
57. Y. Li, Y. Yu, F. Liu, B. Zhang, and G. Shvets, "Topology-controlled photonic cavity based on the near-conservation of the valley degree of freedom," Phys. Rev. Lett. **125**, 213902 (2020).
58. C. Qian, S. Wu, F. Song, K. Peng, X. Xie, J. Yang, S. Xiao, M. J. Steer, I. G. Thayne, C. Tang, Z. Zuo, K. Jin, C. Gu, and X. Xu, "Two-photon Rabi splitting in a coupled system of a nanocavity and exciton complexes," Phys. Rev. Lett. **120**, 213901 (2018).
59. C. Qian, X. Xie, J. Yang, K. Peng, S. Wu, F. Song, S. Sun, J. Dang, Y. Yu, M. J. Steer, L. G. Thayne, K. Jin, C. Gu, and X. Xu, "Enhanced strong interaction between nanocavities and p-shell excitons beyond the dipole approximation," Phys. Rev. Lett. **122**, 087401 (2019).
60. L. He, H. Ji, Y. Wang, and X. Zhang, "Topologically protected beam splitters and logic gates based on two-dimensional silicon photonic crystal slabs," Opt. Express **28**, 34015–34023 (2020).
61. T. Yamaguchi, Y. Ota, R. Katsumi, K. Watanabe, S. Ishida, A. Osada, Y. Arakawa, and S. Iwamoto, "GaAs valley photonic crystal waveguide with light-emitting InAs quantum dots," Appl. Phys. Express **12**, 062005 (2019).